# How Slippery are Piecewise-Constant Coastlines in Numerical Ocean Models?

By ALISTAIR ADCROFT, *Department of Earth, Atmospheric and Planetary Sciences, Massachusetts Institute of Technology 54-1523, Cambridge, Massachusetts 02139, United States*, and DAVID MARSHALL*, *Department of Meteorology, University of Reading, P.O. Box 243, Reading, RG6 6BB, United Kingdom*

*Corresponding author.
email: davidm@met.reading.ac.uk

ABSTRACT

Coastlines in numerical ocean models are oriented at various finite angles to the model grid. Such arbitrarily angled coasts cannot easily be represented in finite difference models. Thus the true coastline is usually replaced by a piecewise-constant approximation in which the model coastline is everywhere aligned with the model grid. Here we study the consequences of the piecewise-constant approximation in an idealised shallow-water ocean model. By rotating the numerical grid at various finite angles to the physical coastlines, we are able to isolate the impact of piecewise-linear boundaries on the model circulation. We demonstrate that piecewise-constant coastlines exert a spurious drag on model boundary currents, dependent on both the implementation of the slip boundary condition and the form of the viscous stress tensor. In particular, when free-slip boundary conditions are applied, the character of the circulation can be reduced to no-slip in the presence of a piecewise-constant boundary. The spurious drag can be avoided in a free-slip limit if the viscous stress tensor is written in terms of vorticity and divergence.

# 1. Introduction

The choice of lateral boundary condition in a numerical ocean model has a profound influence on the separation and recirculation of boundary currents, such as the Gulf Stream, and on the transport of water masses through gaps, such as the Indonesian through-flow. While the appropriate boundary condition for a continuum fluid is "no-slip" (for example, Richarson, 1973), it is less clear that no-slip is appropriate for a finite-resolution ocean model in which a boundary current is barely resolved by the numerical grid. Alternative slippery boundary conditions have been advocated in which the tangential component of the boundary velocity remains finite. The "free-slip" condition is the most wide-spread, in which the tangential shear at the boundary vanishes; "hyper-slip" and "super-slip" conditions have also been proposed to enable advection of vorticity along coastlines. An excellent review of these various boundary conditions, and their impact on the large-scale circulation, is given by Pedlosky, 1996.

Irrespective of the chosen boundary condition, ocean general circulation models (OGCMs) need also to accommodate irregular coastlines which are oriented at finite angles to the model grid. In a typical finite difference model, such coastlines are generally replaced by a piecewise-constant approximation in which the model boundary is everywhere parallel to the model grid (Fig. 1). While the piecewise-constant treatment greatly simplifies numerical implementation of the solid-wall boundary condition, the implications for the slippery character of model coastlines are less clear. For example, where the coastline is oriented at 45° to the model grid, one is effectively setting *both* components of the fluid velocity, $u$ and $v$, to zero within one grid point of each other, even where a slippery boundary condition is prescribed. The aims of this contribution are:

- to demonstrate that piecewise-constant coastlines exert a spurious drag on model boundary currents; and
- to investigate the sensitivity of this spurious drag to the implementation of the slip boundary condition and formulation of the viscous stress tensor.

In section 2, we describe the strategy and formulation of our numerical experiments. In section 3, we present solutions in which the lateral boundary condition is implemented using "ghost points" lying outside the model domain. In section 4, we present solutions in which the boundary condition is instead applied directly to the stress tensor, and we also investigate sensitivity of our results to different formulations of the stress tensor. In section 5, the implications of our results for numerical ocean models are discussed further.

## 2. Numerical model

### *2.1. General approach*

Our approach is to consider the wind-driven circulation in a square ocean basin in which we rotate the numerical grid at various finite angles to the model coastlines, as sketched schematically in Fig. 2. Any differences between solutions at different angles of rotation can thus be attributed to the piecewise-constant nature of the approximated model coastline (we assume that effects associated with anisotropy of the numerical grid are not significant). The wind-stress, $\boldsymbol{\tau} = -\tau_0 \cos(\pi\tilde{y}/L)\tilde{\mathbf{i}}$, and Coriolis parameter, $f = f_0 + \beta\tilde{y}$ are specified as functions of the *physical* coordinates $(\tilde{x}, \tilde{y})$, distinct from the rotated *model* coordinates $(x, y)$ aligned along the numerical grid. The basin is bounded by solid walls at $\tilde{x} = 0,\ L$ and $\tilde{y} = 0,\ L$.

### *2.2. Discretised equations*

The discretised shallow-water equations are written:

$$\partial_t u - \overline{(f+\zeta)}^{y}\overline{v}^{xy} + \partial_x B = \frac{\tau^{(x)}}{\rho_o \overline{h}^{x}} - ru + \nu\nabla^2 u, \tag{1}$$

$$\partial_t v + \overline{(f+\zeta)}^{x}\overline{u}^{xy} + \partial_y B = \frac{\tau^{(y)}}{\rho_o \overline{h}^{y}} - rv + \nu\nabla^2 v, \tag{2}$$

$$\partial_t h + \partial_x(\overline{h}^{x} u) + \partial_y(\overline{h}^{y} v) = 0. \tag{3}$$

Here, $(u, v)$ is the fluid velocity, $h$ is the thickness of the shallow-water layer, $\zeta = \partial_x v - \partial_y u$ is the relative vorticity, $B = g'h + \frac{1}{2}(\overline{u}^{x2} + \overline{v}^{y2})$ is the Bernoulli potential, $g'$ is the reduced gravity, $\rho_o$ is a reference density, $r$ is the coefficient of linear friction, and $\nu$ is the coefficient of lateral eddy viscosity. The model variables are staggered in the form of an Arakawa C-grid. The numerical discretisation of the momentum equations is that of Bleck and Boudra, 1986; the discrete equations conserve mass and enstrophy, but not energy. The discretisation is nominally second-order accurate in space: the grid-spacing is constant and all interpolations and discrete measurements of gradients in the interior of the ocean are centred.

### *2.3. Boundary conditions*

The solid boundaries are placed such that north-south sections of coastline fall on $u$-points, and east-west sections fall on $v$-points. The solid wall boundary condition of no *normal* flow is therefore naturally imposed.

A second boundary condition is required to evaluate the lateral friction and the vorticity at the boundaries. The two alternatives considered here are:

- *no-slip* where the tangential flow is zero on the boundary, and
- *free-slip* where the tangential shear vanishes on the boundary but the tangential flows remains finite.

The free-slip boundary condition is synonymous with the "stress-free" boundary condition in which the tangential stress is set to zero.

In the solutions presented in section 3, the boundary conditions are implemented using "ghost points" lying a half grid point outside the model domain. Along a no-slip boundary, the velocity at the ghost point is set equal and opposite to the interior value, whereas along a free-slip boundary, the ghost

velocity is set equal to the interior value:

$$\begin{array}{lll} \textit{no-slip:} & \overline{v}^x = 0 & \text{(north-south boundary)} \\ & \overline{u}^y = 0 & \text{(east-west boundary)} \\ \textit{free-slip:} & \partial_x v = 0 & \text{(north-south boundary)} \\ & \partial_y u = 0 & \text{(east-west boundary)} \end{array} \tag{4}$$

This convenient approach is widely used in numerical models (for example, Bleck et al., 1992).

An alternative implementation of the boundary conditions applied directly to the viscous stress tensor will be described subsequently in section 4.

### *2.4. Numerical details*

The model parameters used for all experiments are: $L = 2000\,\mathrm{km}$, $f_0 = 0.7 \times 10^{-4}\,\mathrm{s}^{-1}$, $\beta = 2 \times 10^{-11}\,\mathrm{m}^{-1}\,\mathrm{s}^{-1}$, $\nu = 500\,\mathrm{m}^2\mathrm{s}^{-1}$, $r = 10^{-7}\,\mathrm{s}^{-1}$, $\rho_0 = 10^3\,\mathrm{kg\,m}^{-3}$, $g' = 0.02\,\mathrm{m\,s}^{-2}$ and $\tau_o = 0.2\,\mathrm{N\,m}^{-2}$. The initial layer thickness is $h_0 = 500\,\mathrm{m}$.

The grid-spacing is $\Delta x = \Delta y = 25\,\mathrm{km}$, equivalent to $\sim 1/4^\circ$ resolution at midlatitudes. The nominal deformation radius, $L_\rho = \sqrt{g'h_0}/f_0 \approx 45\,\mathrm{km}$, is resolved by the grid, and the wave resolution parameter, $2L_\rho/\Delta x \sim 3.6$, ensures the discrete inertia-gravity waves are properly dispersive. The Munk boundary layer scale, $(\nu/\beta)^{1/3} \sim 30\,\mathrm{km}$, is barely resolved (in keeping with the majority of present-day OGCMs). The third order Adams-Bashforth (III) time-stepping scheme is used with a time-step of $\Delta t = 0.25$ hours. All experiments are integrated for 10 years from a state of rest, after which time each is converging towards either a steady state or a statistically-steady limit cycle.

# 3. Results

## *3.1. Solutions on a non-rotated grid*

First we consider the solutions obtained on a non-rotated grid that is parallel to the model coastlines. The structure of the gyre is singularly sensitive to the choice of no-slip or free-slip lateral boundary condition (Blandford, 1971). Figure 3 illustrates this point by showing snapshots of the fluid depth, $h$, after ten years of integration with (a) no-slip boundary conditions, and (b) free-slip boundary conditions. Here, the boundary conditions are implemented using the method of ghost points described above. In each case the solutions are converging towards a steady state.

The "no-slip " solution (Fig. 3a) is characterised by a Sverdrup interior, an inertial boundary current along the western margin of the basin, and a standing eddy in the north-west corner of the basin. A standing Rossby wave is superimposed on the Sverdrup interior and decays away from the western boundary. The transport of the recirculating gyre is approximately 35 Sv.

The "free-slip" solution (Fig. 3b) is also composed of a Sverdrup interior and an inertial boundary current along the western margin, but now with an extended inertial recirculation sub-gyre across the northern margin of the basin. The latter enhances the gyre transport to 70 Sv, considerably in excess of the 30 Sv predicted by Sverdrup balance (Sverdrup, 1947). Observations indicate that the transport of the Gulf Stream increases from 30 Sv off the coast of Florida (Niiler and Richardson, 1973) to 85 Sv at Cape Hatteras (Worthington, 1972), broadly consistent with the free-slip solution. The eastward-flowing jet, representing the separated Gulf Stream, penetrates approximately 1700 km along the northern edge of the gyre

The above solutions are characteristic of the classical "no-slip" (Bryan, 1963) and "free-slip" (Veronis, 1966) circulations, and serve as the "control experiments" against which we now compare results obtained on rotated model grids.

The above experiments are repeated under identical conditions except that the model grid is rotated at three finite angles to the coastlines, which therefore assume a piecewise-constant appearance. Fig. 4 shows the layer thickness, $h$, after 10 years of integration using both no-slip (left panels) and free-slip (right panels) boundary conditions, on grids rotated at 5° (top row), 10° (middle row) and 45° (bottom row) relative to the coastlines.

For small angles of rotation, the no-slip solutions (left panels) are broadly consistent with the control simulation in Fig. 3a. The characteristic tight recirculating sub-gyre in the northwest corner is retained along with the standing Rossby wave decaying away from the western boundary current. At 45° rotation, however, the inertial boundary current separates prematurely from the western boundary (bottom left panel), and the recirculating eddy in intensified. The separation point is not steady, but settles into a limit cycle, migrating approximately 100km up and down the coastline.

In contrast, the free-slip solutions are fundamentally altered for all angles of rotation, even as small as 5° . In each case, including negative angles of rotation (not shown), the circulation assumes the character of the classical no-slip limit. Thus the introduction of piecewise-constant coastlines appears to represent a singular perturbation on the structure of the free-slip solution in these experiments.

On the grid rotated at 45° , the free-slip and no-slip solutions are exactly identical which clearly contradicts the use of different boundary conditions in each. To understand this behaviour, consider the numerical integration of the $v$ momentum equation, (2), adjacent to a western boundary. On a non-rotated grid (Fig. 5a), the ghost points are used to evaluate both the lateral friction term, $-\nu\nabla^2 v$, half a grid-point inside the boundary, and the vorticity, $\zeta$, at the boundary. On the rotated grid (Fig. 5b), however, one is able to evaluate both terms without using ghost points. No viscous boundary condition is therefore used along the piecewise-constant coastline oriented at 45° .

To obtain a quantitative estimate of the error incurred on the rotated grid, consider the ideal scenario of an initial semi-infinite current with a uniform northward velocity $\tilde{v} = \sqrt{2}U$, adjacent to a western boundary. If the layer thickness, $h$, can be considered constant at leading order, then the net viscous deceleration of the current per unit length of coastline (measured in the $\tilde{y}$ direction) is simply

$$\mathcal{D} = \frac{\int_{\tilde{y}} \int_{0}^{\infty} \rho_0 \nu \nabla^2 \tilde{v} \, d\tilde{x} \, d\tilde{y}}{\int_{\tilde{y}} d\tilde{y}}. \tag{5}$$

We identify $\mathcal{D}$ as the "net viscous stress" acting on the current, incorporating both a tangential (shear) stress and normal (form) stress.

On the non-rotated grid (Fig. 5a), the only contribution is from the $v^+$ velocity points adjacent to the coastline, giving

$$\begin{array}{ll} \textit{no-slip:} & \mathcal{D} = -2\sqrt{2}\rho_0 \nu U \,/\, \Delta x, \\ \textit{free-slip:} & \mathcal{D} = 0. \end{array} \tag{6}$$

On the grid rotated at 45° (Fig. 5b), we must consider the viscosity at both the $u^+$ and $v^+$ velocity points where $\nu\nabla^2 u = -2\nu U/(\Delta x)^2$, $\nu\nabla^2 v = -2\nu U/(\Delta x)^2$ respectively. Projecting onto the $\tilde{y}$ axis then gives,

$$\mathcal{D} = -2\rho_0 \nu U \,/\, \Delta x, \tag{7}$$

identical for both no-slip and free-slip boundary conditions.

The net viscous stress is therefore underestimated by a factor $\sqrt{2}$ along the no-slip boundary rotated at 45° , consistent with the enhanced gyre transport observed in the numerical solution (Fig. 4). Along the free-slip boundary, the viscous stress is finite whereas it should be zero, again consistent with the numerical results.

## 4. Boundary conditions applied to stress tensor

The results of section 3 indicate that spurious frictional stresses are exerted along piecewise-constant boundaries where the boundary conditions are implemented using ghost points. We now investigate the possibility that these problems might be avoided by applying the no-slip/free-slip boundary condition directly to the viscous stress tensor to ensure the correct boundary stress.

### *4.1. Stress tensor formulations*

First, we rewrite the lateral friction term in the momentum equations, (1) and (2), as the divergence of stresses,

$$\begin{aligned} \nu\nabla^2 u &\rightarrow \partial_x F^{ux} + \partial_y F^{uy}, \\ \nu\nabla^2 v &\rightarrow \partial_x F^{vx} + \partial_y F^{vy}, \end{aligned}$$

where

$$\boldsymbol{F} = \begin{pmatrix} F^{ux} & F^{uy} \\ F^{vx} & F^{vy} \end{pmatrix}.$$

is the viscous stress tensor.[1] Following Batchelor, 1967, we refer to $F^{ux}$ and $F^{vy}$ as "normal" stresses, and $F^{uy}$ and $F^{vx}$ as "tangential" stresses. Three forms of $\boldsymbol{F}$ are considered here:

- the *conventional* form,

$$\boldsymbol{F_{conv}} = \begin{pmatrix} \nu\partial_x u & \nu\partial_y u \\ \nu\partial_x v & \nu\partial_y v \end{pmatrix}, \tag{8}$$

- the *symmetric* form,

$$\boldsymbol{F_{sym}} = \begin{pmatrix} \nu(\partial_x u - \partial_y v) & \nu(\partial_y u + \partial_x v) \\ \nu(\partial_y u + \partial_x v) & -\nu(\partial_x u - \partial_y v) \end{pmatrix}, \tag{9}$$

[1] Note that $\boldsymbol{F}$ must be multiplied by the density $\rho_0$ to give a force per unit area.

- and the *vorticity-divergence* form,

$$\boldsymbol{F}_{\boldsymbol{\zeta},\boldsymbol{D}} = \begin{pmatrix} \nu(\partial_x u + \partial_y v) & -\nu(\partial_x v - \partial_y u) \\ \nu(\partial_x v - \partial_y u) & \nu(\partial_x u + \partial_y v) \end{pmatrix}. \tag{10}$$

The conventional form (8) is the most widely used in ocean models. However, compelling arguments in favour of the symmetric form (9) have been given by Shchepetkin and O'Brien, 1996, the essential points being that the Reynolds stress tensor is symmetric ($\overline{u'v'} = \overline{v'u'}$) and that a non-zero antisymmetric component leads to non-conservation of angular momentum (Batchelor, 1967; Panton, 1996). The vorticity-divergence form (10) is antisymmetric (for example, Madec et al., 1991) but is useful in allowing selective dissipation of gravity-waves through different viscosities acting on vorticity and divergence.

All three forms of the stress tensor give rise to the same dissipation in the continuous momentum equations; that is, expanding the divergence of the tensor, the actual dissipation is $\boldsymbol{\nabla}.\boldsymbol{F} = \nu\nabla^2\mathbf{u}$ in each case. However, at the discrete level the three forms can possess different properties adjacent to model coastlines.

### *4.2. Implementation of boundary conditions*

The normal stresses ($F^{ux}$ and $F^{vy}$) can be evaluated adjacent to boundaries without additional boundary conditions. However the tangential stresses fall on the boundary and must be specified through a boundary condition. On free-slip boundaries, we reinterpret "free-slip" to mean "stress-free" and set the tangential stress to zero:

$$\begin{array}{lll} \textit{free-slip:} & F^{vx} = 0 & \text{(north-south boundary)} \\ & F^{uy} = 0 & \text{(east-west boundary)} \end{array} \tag{11}$$

On no-slip boundaries, the velocity shear is made proportional to the interior tangential flow:

$$\begin{array}{lll} \textit{no-slip:} & \partial_x v = -2v^+/\Delta x & \text{(north-south boundary)} \\ & \partial_y u = -2u^+/\Delta y & \text{(east-west boundary)} \end{array} \tag{12}$$

where $u^+$, $v^+$ refer to the tangential velocity components a distance $\Delta x/2$ inside the boundary. These components of velocity shear are then used to evaluate the tangential stress on the boundary which will depend on the particular form of stress tensor. On a non-rotated grid, the above lead to the same tangential stress as in the previous section, irrespective of the form of stress tensor. Note that the no-slip boundary condition essentially involves a side-difference which is only $O(\Delta x)$ accurate (Shchepetkin and O'Brien, 1996). For the free-slip boundary condition, however, the statement of zero tangential stress on the boundary is exact and does not incur a loss of accuracy.

The discretised model also requires the vorticity on the boundary to evaluate the nonlinear terms in the momentum equations. On a no-slip boundary the velocity shears are specified in the lateral boundary conditions (12) from which the vorticity follows directly. On a free-slip boundary, we set the relative vorticity to zero, consistent with the experiments presented in section 3 (here we are implicitly neglecting any vorticity associated with curvature of the boundary).

### *4.3. Numerical results*

For all three forms of stress tensor, the solutions obtained on a non-rotated grid are identical to those obtained previously using ghost points (Fig. 3). We now present solutions after 10 years of integration on grids rotated at 10° , 30° and 45° .

Solutions obtained using the *conventional* form of stress tensor are shown in Fig. 6 for no-slip (left panels) and free-slip (right panels) boundary conditions. The no-slip solutions are similar to those obtained using ghost points; in particular there is a tendency for premature boundary current separation at large angles of rotation. However, the free-slip solutions differ markedly from those obtained using ghost points. The solution on the 10° grid is of classical free-slip character. The gyre contains an extended inertial recirculation along its northern margin, although its penetration is somewhat reduced from that on the non-rotated grid. On the 30° grid, the penetration of the subgyre is much reduced, and on the 45° grid the solution is closer to the classical no-slip limit. In contrast to Fig. 4, the 45° no-slip and free-slip circulations are no

longer identical.

Solutions obtained using the *symmetric* stress tensor are shown in Fig. 7. The behaviour of the no-slip solutions is very much as for the conventional stress tensor; the boundary current separates progressively further south as the angle of rotation is increased. The free-slip solutions are more affected by the rotation of the grid than in the case of the conventional stress tensor.

Finally, solutions obtained using the *vorticity-divergence* $(\zeta - D)$ form of the stress tensor are shown in Fig. 8. Again, the no-slip solutions exhibit a tendency towards early separation at large angles of rotation. However, the free-slip solutions are far less affected by the rotation of the grid. The penetration of the inertial recirculation is diminished with increasing angle and the strength of the subgyre is increased beyond that obtained in the non-rotated solutions. Nevertheless, the solution is of classical free-slip character for all three angles of rotation.

### *4.4. Thought experiment*

To explain these results we return to the thought experiment of section 3.3 in which we consider a uniform northward current, $\tilde{v} = \sqrt{2}U$, adjacent to a western boundary on a grid rotated at 45° . As in section 3.3, we define the "net viscous stress" as the net viscous deceleration of the current per unit length of coastline (measured in the $\tilde{y}$ direction),

$$\mathcal{D} = \frac{\int_{\tilde{y}} \int_{0}^{\infty} \rho_0 (\boldsymbol{\nabla}.\boldsymbol{F}).\tilde{\mathbf{j}}\, d\tilde{x}\, d\tilde{y}}{\int_{\tilde{y}} d\tilde{y}}. \tag{13}$$

First consider the *no-slip* limit. The tangential and shear stresses are everywhere zero except at the points on and adjacent to the boundary (indicated by the symbol + on Fig. 9). Below we list the two active components of the stress tensor acting on the $v$ momentum equation (similar terms act on the $u$

momentum equation), and the net viscous stress:

$$\begin{array}{lccc} & F^{vx+} & F^{vy+} & \mathcal{D} \\ \textit{conventional:} & 2\nu U \,/\, \Delta x & -\nu U \,/\, \Delta x & -3\rho_0 \nu U \,/\, \Delta x, \\ \textit{symmetric:} & 0 & -2\nu U \,/\, \Delta x & -2\rho_0 \nu U \,/\, \Delta x, \\ \zeta - D: & 4\nu U \,/\, \Delta x & 0 & -4\rho_0 \nu U \,/\, \Delta x. \end{array} \tag{14}$$

For comparison, recall that $\mathcal{D} = -2\sqrt{2}\rho_0 \nu U \,/\, \Delta x$ on a non-rotated grid. Thus we see that the net viscous stress is underestimated using the symmetric form of the stress tensor, overestimated using the vorticity-divergence form, and is slightly underestimated using the conventional form. The net viscous stress is due to a different combination of normal and tangential stresses in each case.

Now consider the *free-slip* limit in which we find:

$$\begin{array}{lccc} & F^{vx+} & F^{vy+} & \mathcal{D} \\ \textit{conventional:} & 0 & -\nu U \,/\, \Delta x & -\rho_0 \nu U \,/\, \Delta x, \\ \textit{symmetric:} & 0 & -2\nu U \,/\, \Delta x & -2\rho_0 \nu U \,/\, \Delta x, \\ \zeta - D: & 0 & 0 & 0. \end{array} \tag{15}$$

Here, the net viscous stress should be zero, but this is only the case with the vorticity-divergence form of the stress tensor. The tangential stresses are correctly zero in each case. However, the appearance of finite normal stresses indicates that a spurious form drag is being exerted on the current by the roughness of the piecewise-constant boundary. This spurious form drag is avoided only if one employs the vorticity–divergence form of the stress tensor.

## 5. Discussion

Our analysis and numerical results suggest the following points:

- Piecewise-constant coastlines exert a spurious stress on model boundary currents, dependent on both the choice and implementation of the lateral boundary condition.
- Where the boundary condition is implemented using ghost points, the boundary stress is underestimated along a no-slip coastline, and is finite

along a free-slip coastline. Further, the viscous boundary condition is not used on a piecewise-coastline oriented at 45° to the model grid.

- Even where the boundary condition is applied directly to the tangential boundary stress, the numerical roughness inherent in the piecewise-constant approximation nevertheless exerts a spurious form drag on the fluid. Use of the vorticity-divergence form of viscous stress tensor avoids this spurious form drag.

We have focussed in this paper exclusively on experiments in which the width of the no-slip sublayer is comparable to the horizontal grid spacing (as is the case in the majority of OGCM studies reported in the literature). However our conclusion that piecewise-constant coastlines exert a spurious form drag on model boundary currents appears to hold even where the boundary layer is resolved by several grid points. Figure 10 shows results obtained on a grid rotated at 45° where the grid spacing has been reduced to $\Delta x = 6.25$ km (four times finer resolution than used throughout the paper); no-slip and free-slip solutions are shown in the left and right columns respectively. The no-slip solutions are virtually identical for all three forms of stress tensor and the boundary current no longer separates prematurely. However with free-slip boundary conditions applied, the conventional and symmetric tensor solutions are devoid of a large-amplitude penetrative inertial recirculation—even at this resolution, the spurious form drag associated with the piecewise-constant coastlines appears to modify the character of a free-slip solution towards the classical no-slip limit. Only the vorticity-divergence tensor solution, in which the spurious stresses are eliminated, shows the correct behaviour.[2]

We have also performed a number of additional experiments exploring sensitivity to the frictional coefficients, the surface wind stress and domain size; in particular, we have explored a number of alternative finite-difference formulations including an energy-conserving version of the C-grid model and also a B-grid discretisation. In all instances, we obtain similar results to those

[2]Recent work by Verron and Blayo, 1996 suggests that if the eddy viscosity is also reduced to approximately $50\mathrm{m}^2\,\mathrm{s}^{-1}$ and the no-slip sublayer is properly resolved, then the no-slip solution converges towards the classical free-slip limit. Thus at *very* high resolution, while we would expect spurious form stresses along piecewise-constant coastlines to remain, their impact on the structure of the circulation is likely to be reduced.

reported in detail here.

A notorious failing of OGCMs is their inability to correctly model the separation of boundary currents, such as the Gulf Stream. A pervasive feature of many of such models is the presence of a large-amplitude standing eddy adjacent to the separation point (see, for example, Dengg et al., 1996). Free-slip boundary conditions in principle allow for a more penetrative separated boundary current devoid of such an eddy. However our results show that even when the free-slip boundary condition is used, the circulation can be reduced to a no-slip character in the vicinity of piecewise-constant coastlines. Our results suggest that the behaviour of free-slip solutions might be improved if the stress tensor is formulated in terms of vorticity and divergence. While the vorticity-divergence form leads to non-conservation of angular momentum (Batchelor, 1967), there seems little purpose in using an angular momentum-conserving symmetric tensor if spurious form stresses are subsequently generated at the coastlines.

The impact of piecewise coastlines may be reduced in the presence of a coastal topographic slope that will tend to displace the boundary current away from the coast and thus possibly shield it from the difficulties at the boundary. Nevertheless, we believe that ocean modellers need to reconsider the treatment of coastlines in OGCMs. Several promising approaches have been suggested, including finite elements (for example, Myers and Weaver, 1995) and shaved cells (Adcroft et al., 1997); these should be fully investigated. The ultimate goal should be to develop an ocean model in which the circulation is insensitive to the orientation of the numerical grid.

## 6. Acknowledgements

The comments of two anonymous reviewers have resulted in a significantly improved manuscript. We are grateful for financial support from the University of Reading Research Board (DPM) and the UCAR Fellowship Program in Ocean Modelling (AA).

# REFERENCES


Adcroft, A. J., Hill, C. N., and Marshall, J. C. 1997. Representation of topography by shaved cells in a height coordinate ocean model. *Month. Weath. Rev.*, **125**, (in press).

Batchelor, G. K. 1967. *An Introduction to Fluid Dynamics*. Cambridge Univ. Press.

Blandford, R. R. 1971. Boundary conditions in homogeneous ocean models. *Deep Sea Res.*, **18**, 739–751.

Bleck, R. and Boudra, D. 1986. Wind-driven spin-up in eddy resolving ocean models formulated in isopycnal and isobaric coordinates. *J. Geophys. Res.*, **91**, 7611–7621.

Bleck, R., Rooth, C., Hu, D., and Smith, L. 1992. Salinity-driven thermocline transients in a wind- and thermohaline-forced isopycnic coordinate model of the North Atlantic. *J. Phys. Oceanogr.*, **22**, 1486–1505.

Bryan, K. 1963. A numerical investigation of a non-linear model of a wind-driven ocean. *J. Atmos. Sci.*, **20**, 594–606.

Dengg, J., Beckmann, A., and Gerdes, R. 1996. The Gulf Stream separation problem. In: *The Warmwatersphere of the North Atlantic*, (ed. Krauss, W.). Gebruder Borntrager. Berlin.

Madec, G., Chartier, M., Delecluse, P., and Crepon, M. 1991. A Three-Dimensional Numerical Study of Deep-Water Formation in the Northwestern Mediterranean Sea. *J. Phys. Oceanogr.*, **21**(9), 1349–1371.

Myers, P. and Weaver, A. 1995. A diagnostic barotropic finite-element ocean circulation model. *J. Atmos. Oceanic Technol.*, **12**, 511–526.

Niiler, P. and Richardson, W. 1973. Seasonal variability of the Florida Current. *J. Mar. Res.*, **31**, 144–167.

Panton, R. L. 1996. *Incompressible Flow*. John Wiley & Sons, 2nd edition.

Pedlosky, J. 1996. *Ocean Circulation Theory*. Spinger-Verlag.

Richarson, S. 1973. On the no-slip boundary condition. *J. Fluid Mech.*, **59**, 707–719.

Shchepetkin, A. F. and O'Brien, J. J. 1996. A Physically Consistent Formulation of Lateral Friction in Shallow Water Equation Ocean Models. *Month. Weath. Rev.*, **124**, 1285–1298.

Sverdrup, H. U. 1947. Wind-driven currents in a baroclinic ocean; with application to the equatorial currents of the eastern Pacific. *Proc. Nat. Acad. Sci. U.S.*, **33**, 318–326.

Veronis, G. 1966. Wind-driven ocean circulation–Part 2. Numerical solutions of the non-linear problem. *Deep Sea Res.*, **13**, 31–55.

Verron, J. and Blayo, E. 1996. The no-slip condition and the separation of western boundary currents. *J. Phys. Oceanogr.*, **26**, 1938–1951.

Worthington 1972. Comparison between the deep sections across the Kuroshio and the Florida Current and Gulf Stream. In: *Kuroshio, its Physical Aspects*, (ed. Stommel, H.). Univ. Tokyo Press, 371–385.

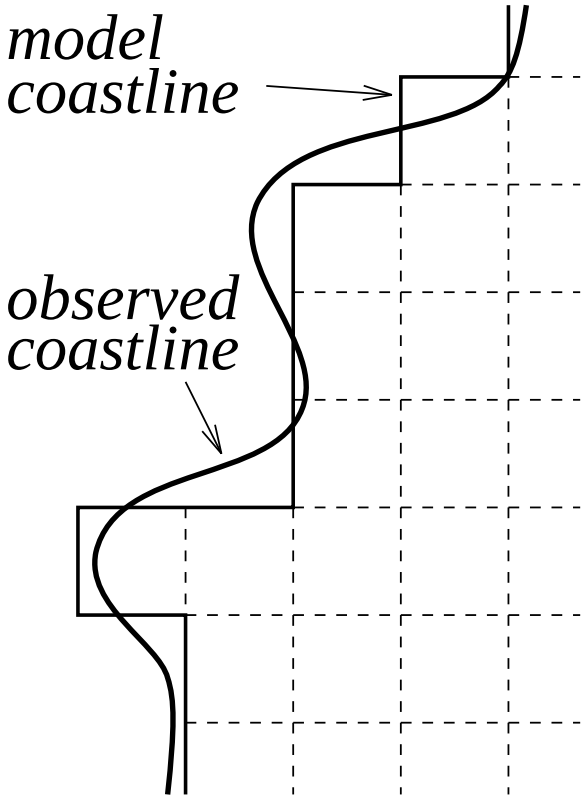


Fig. 1. A schematic diagram illustrating how observed coastlines are replaced by piecewise-constant approximations in numerical models. The thick solid line is the true coastline, the thin solid line is the approximated model coastline, and the dashed lines indicate the grid cells.

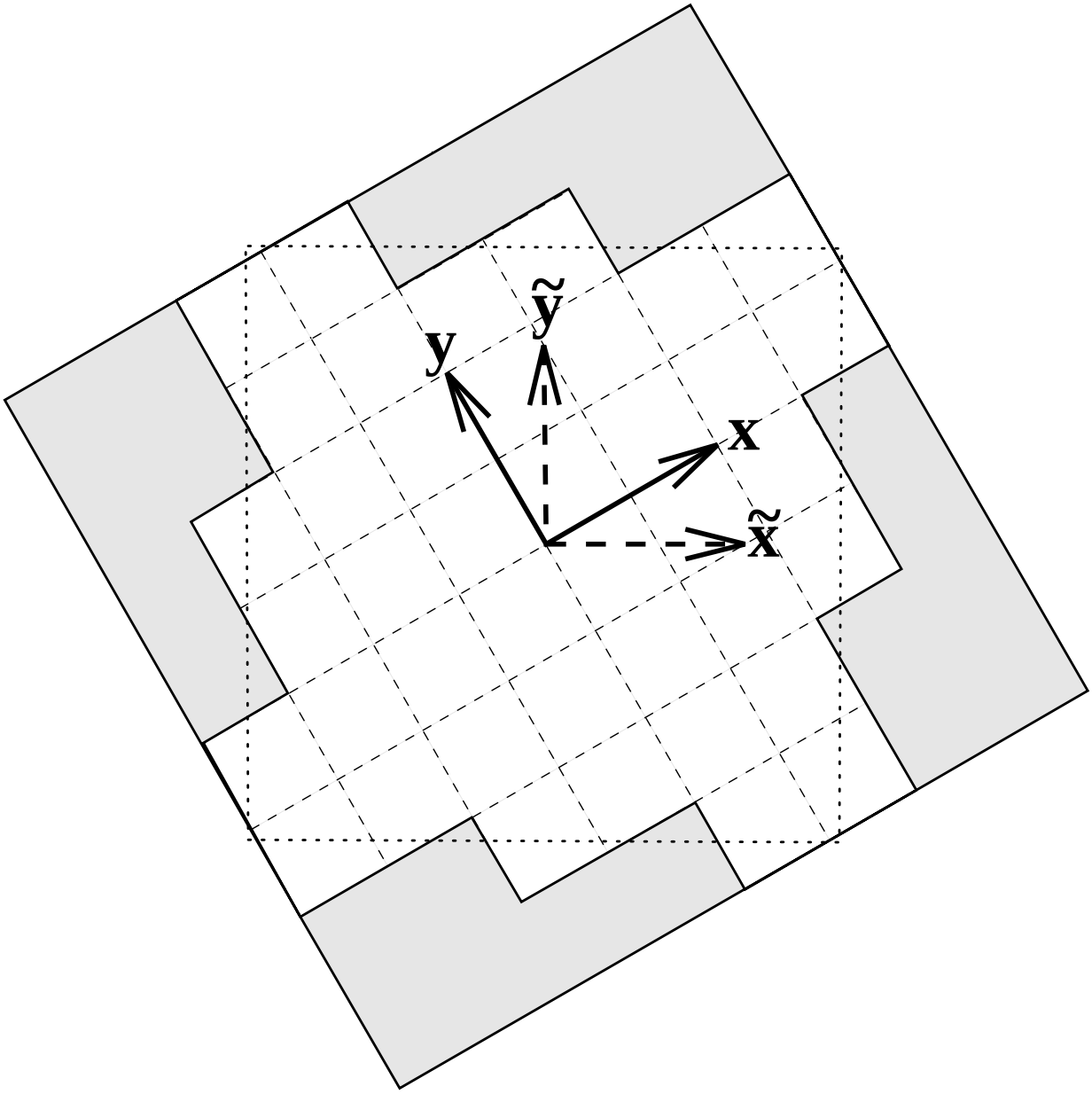


Fig. 2. The model domain is restricted to square region, dimension 2000 km $\times$ 2000 km, masked out from a rotated model grid. The physical coordinates $(\tilde{x}, \tilde{y})$ are distinct from the rotated model coordinates $(x, y)$. The model coastlines assume a piecewise-constant appearance as shown.

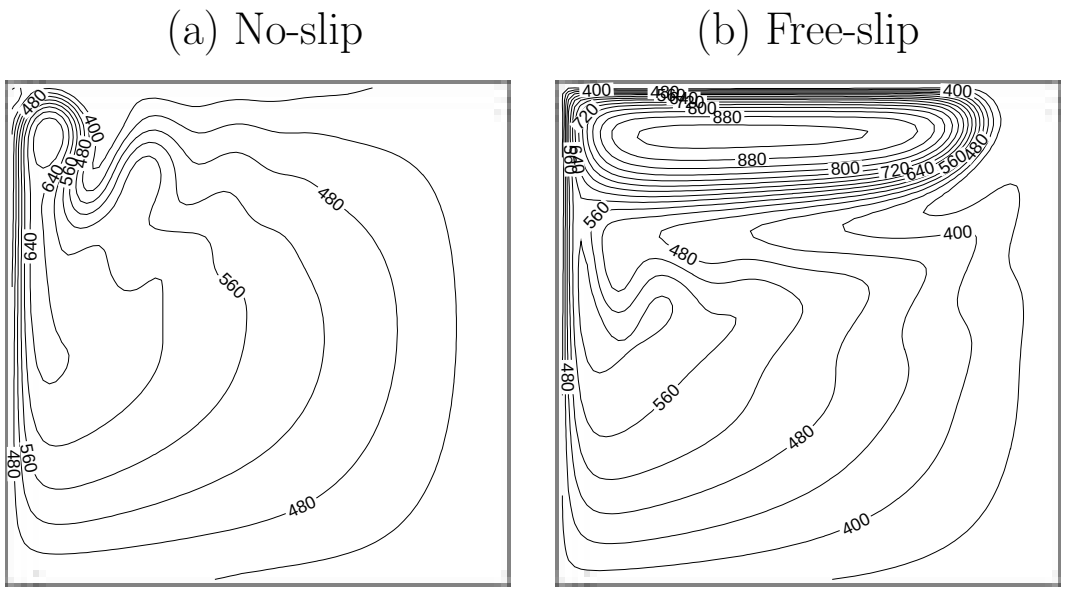


Fig. 3. Instantaneous layer thickness, $h$ (meters), after 10 years with (a) no-slip and (b) free-slip boundary conditions on a non-rotated grid. The contours are streamlines for the geostrophic flow.

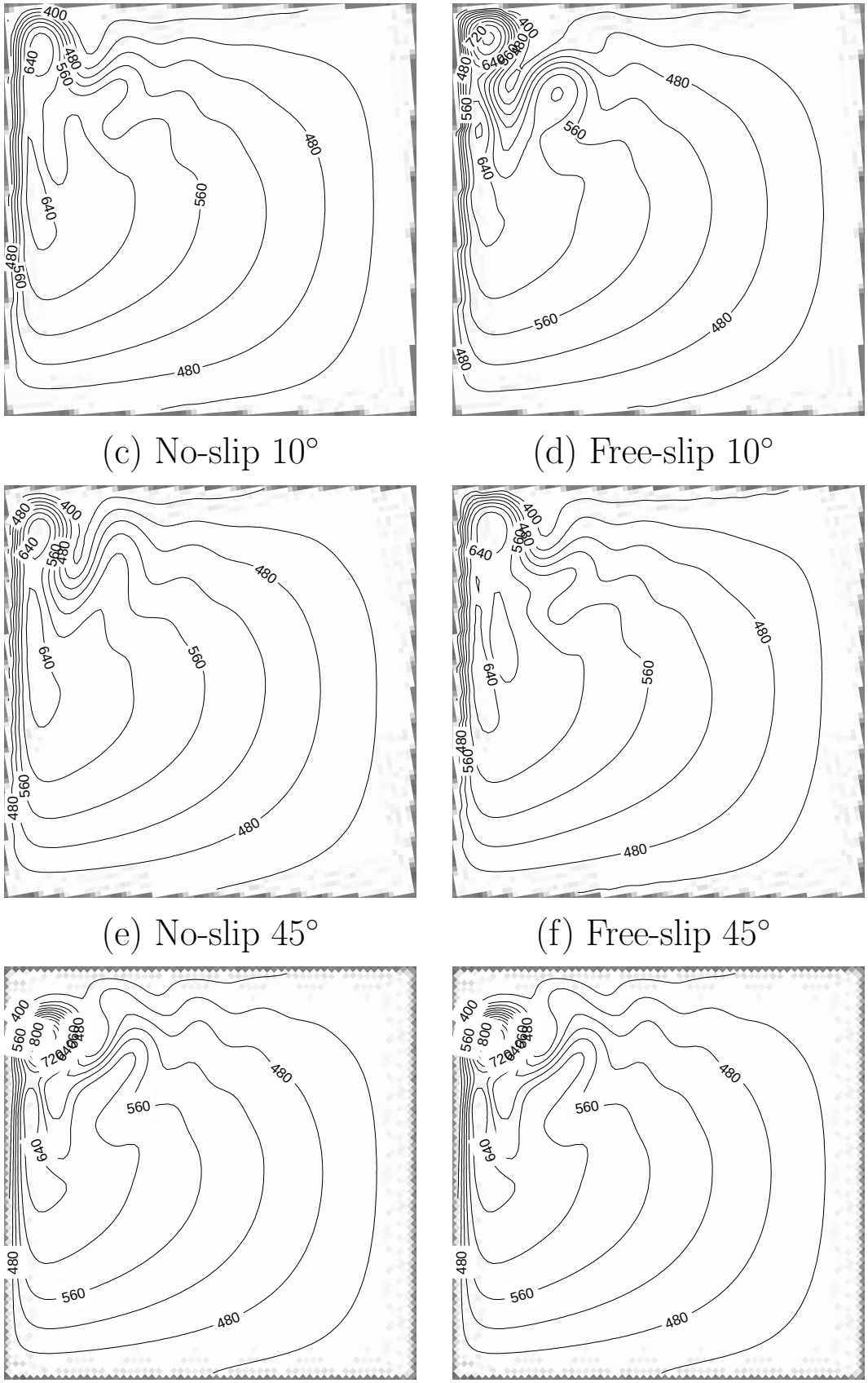


Fig. 4. Instantaneous layer thickness, $h$ (meters), after 10 years on grids rotated at 5° , 10° , and 45° , and boundary conditions implemented using ghost points.

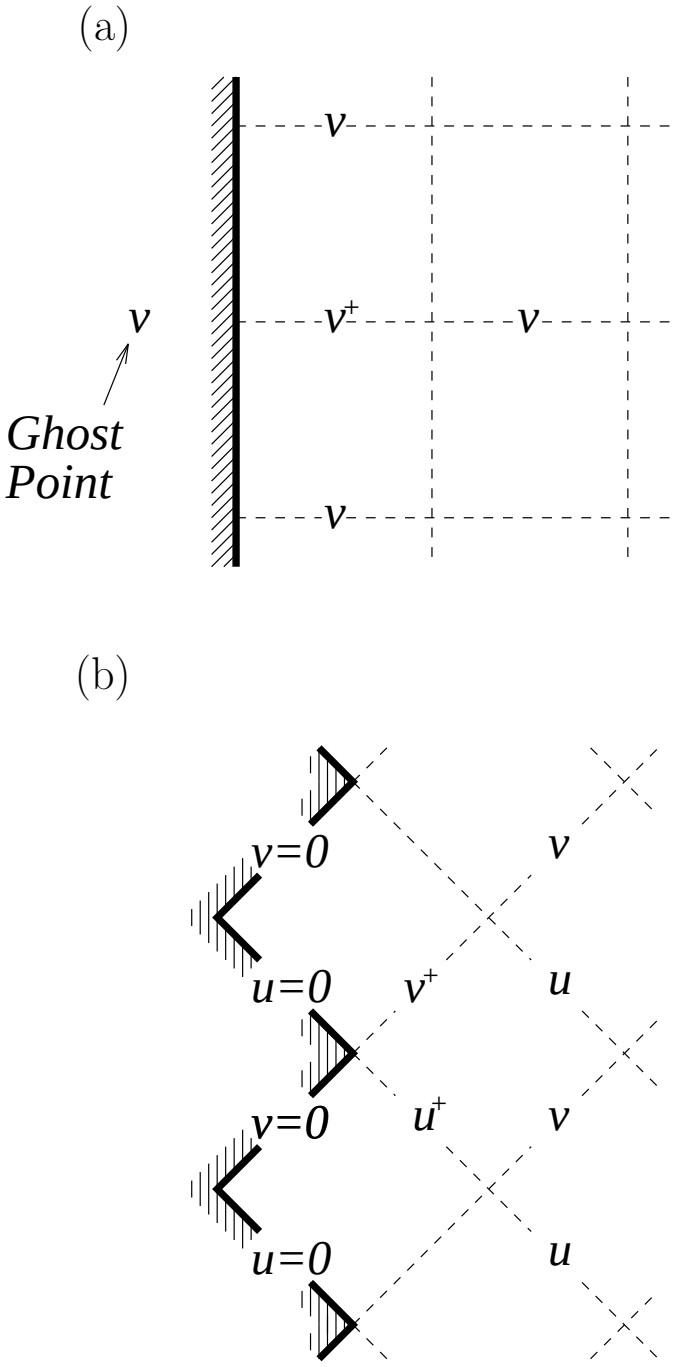


Fig. 5. A schematic showing the distribution of velocity points adjacent to a north-south boundary on (a) and unrotated grid, and (b) a grid rotated at 45/Deg. On the non-rotated grid, the ghost point is used to solve the $v$ momentum equation at the point marked $v^+$. On the rotated grid, however, no ghost point is used.

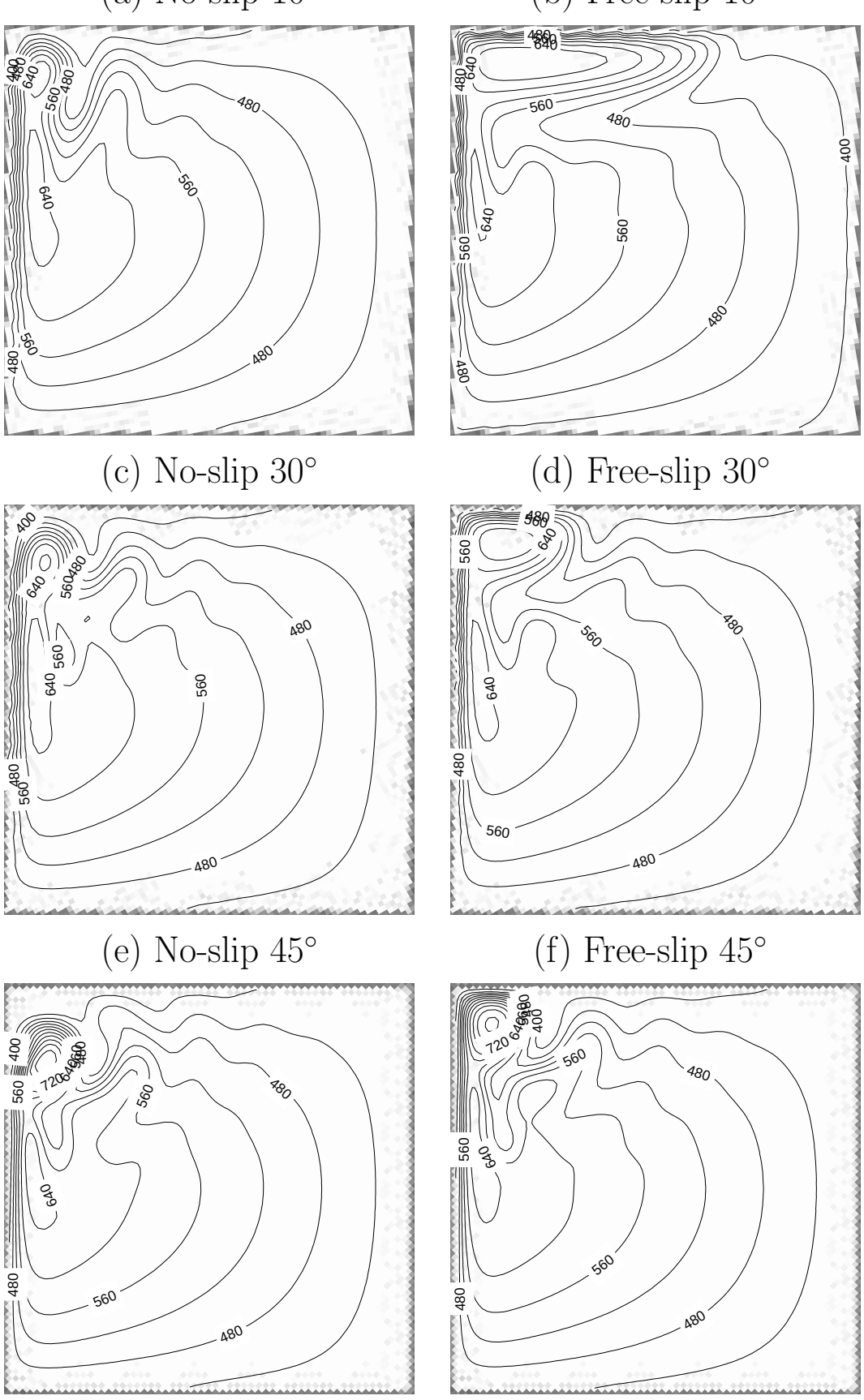


Fig. 6. Instantaneous layer thickness, $h$ (meters), after 10 years, from integrations with the conventional form of the viscous stress tensor.

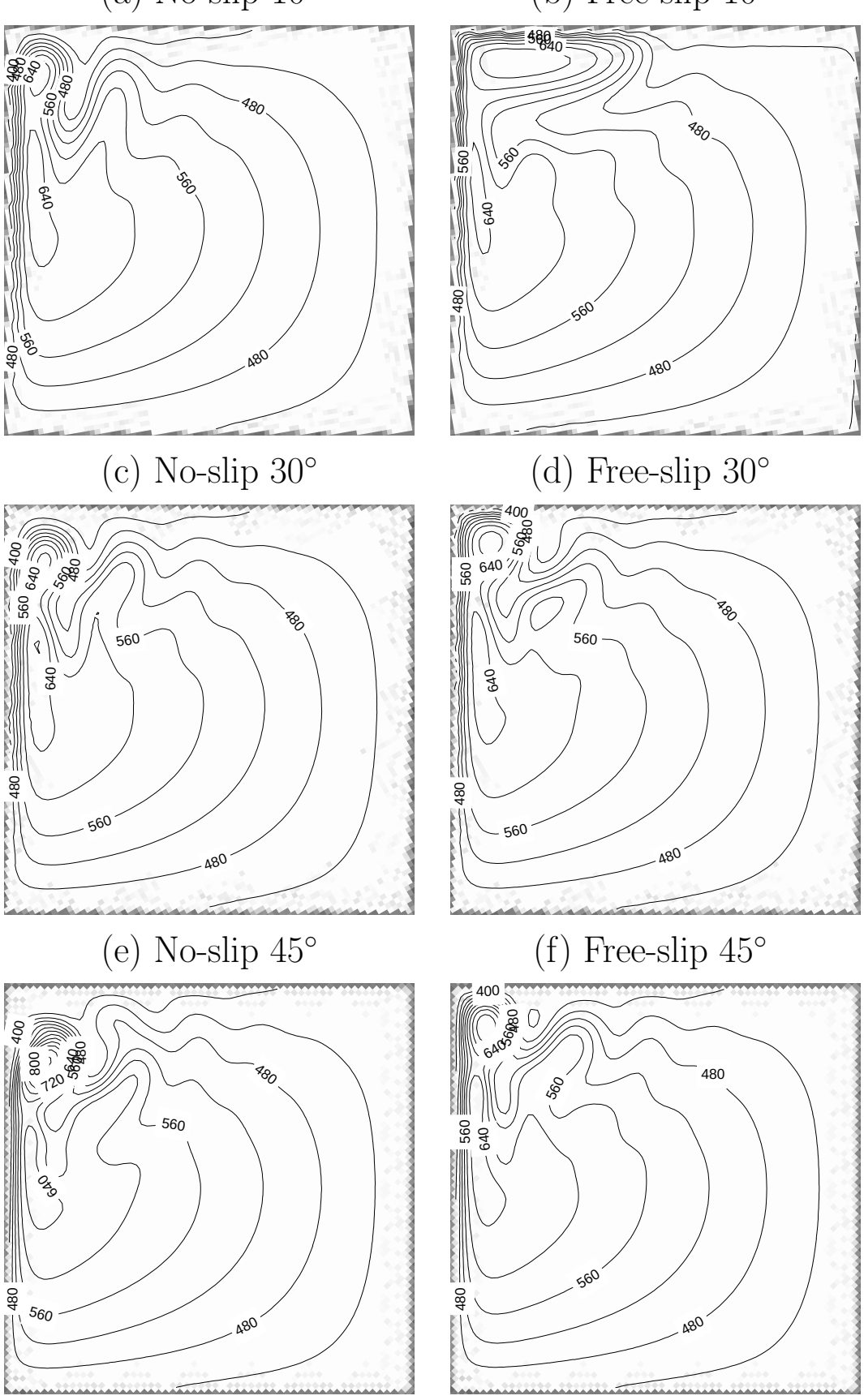


Fig. 7. Instantaneous layer thickness, $h$ (meters), after 10 years, from integrations using the symmetric form of the viscous stress tensor.

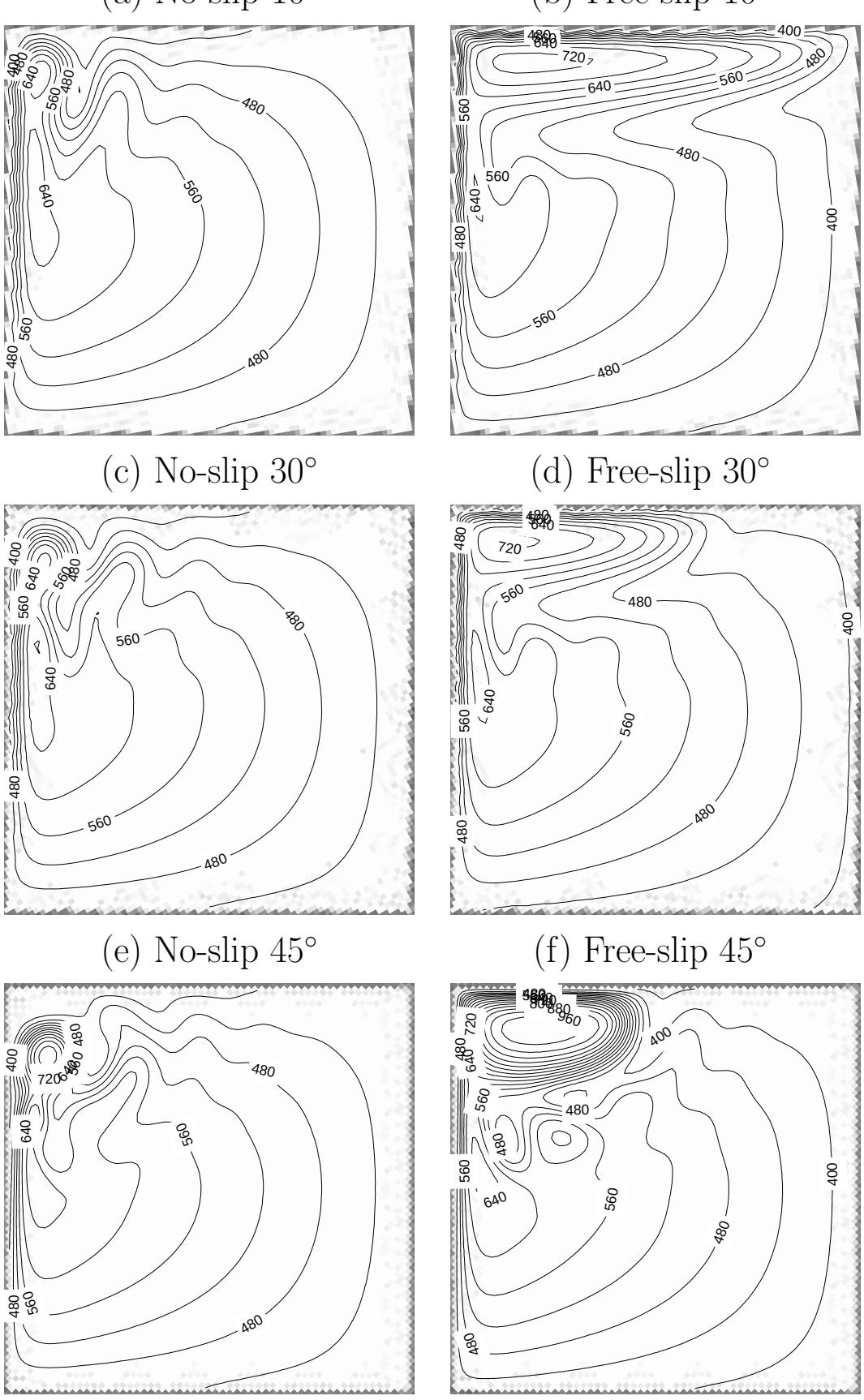


Fig. 8. Instantaneous layer thickness, $h$ (meters), after 10 years, from integrations using the vorticity-divergence form of the viscous stress tensor.

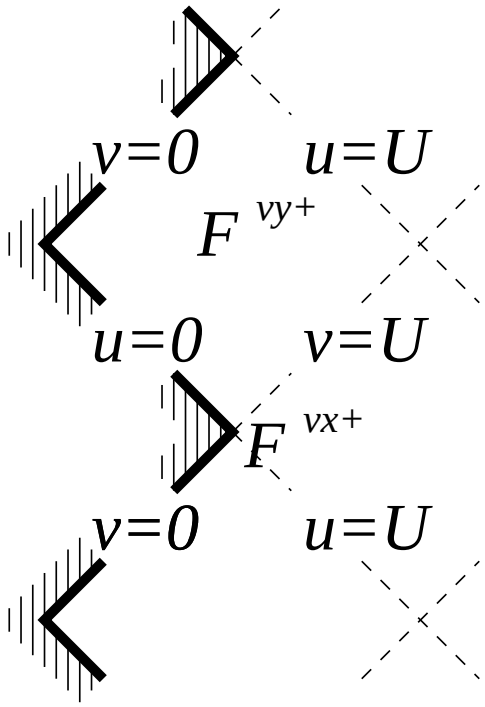


Fig. 9. Schematic diagram showing the placement of the tangential and normal stresses, $F^{vx+}$ and $F^{vy+}$, adjacent to the coastline on a grid rotated at 45° . Also shown are the velocity values for the thought experiment described in the text.

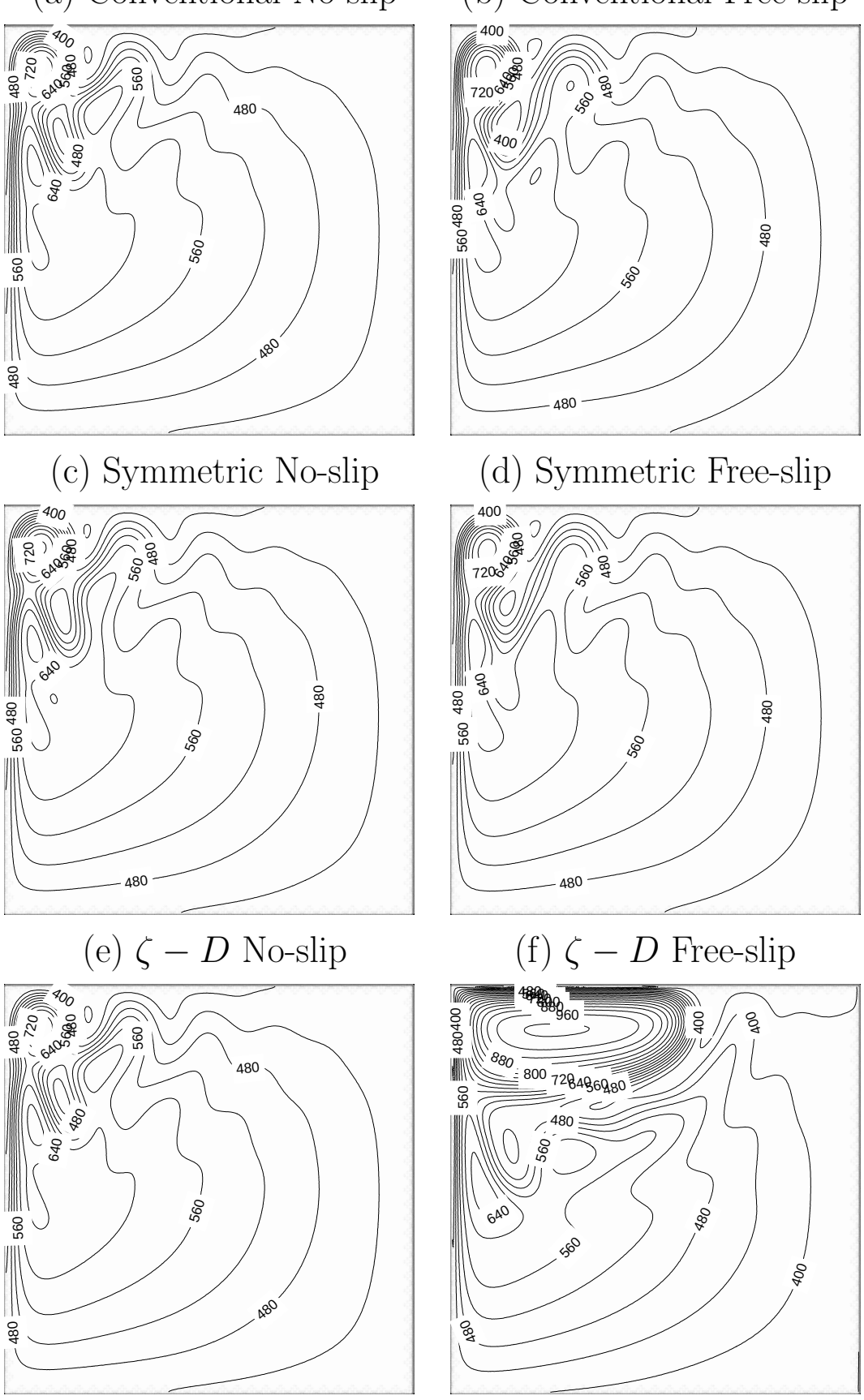


Fig. 10. Instantaneous layer thickness, $h$ (meters), after 10 years, on a grid rotated at 45° with quadruple spatial resolution ($\Delta x = 6.25$ km).